AGU PUBLICATIONS

JGR

Journal of Geophysical Research: Oceans

RESEARCH ARTICLE

10.1002/2014JC010425

Hydrodynamic and sediment transport modeling of New River Inlet (NC) under the interaction of tides and waves

Jia-Lin Chen[1], Tian-Jian Hsu[1], Fengyan Shi[1], Britt Raubenheimer[2], and Steve Elgar[2]

[1]Center for Applied Coastal Research, University of Delaware, University of Delaware, Newark, USA, [2]Applied Ocean Physics and Engineering Department, Woods Hole Oceanographic Institute, Woods Hole, Massachusetts, USA

Key Points:
- The model validated with observed waves and circulation at 30 locations
- A sharp transition of waves and currents on ebb tidal deltas
- Waves generate vortices and landward-directed currents

Correspondence to:
J.-L. Chen,
jialin@udel.edu

Citation:
Chen, J.-L., T.-J. Hsu, F. Shi, B. Raubenheimer, and S. Elgar (2015), Hydrodynamic and sediment transport modeling of New River Inlet (NC) under the interaction of tides and waves, *J. Geophys. Res. Oceans*, , 4028–4047, doi:10.1002/2014JC010425.

Received 4 SEP 2014
Accepted 27 APR 2015
Accepted article online 4 MAY 2015
Published online 7 JUN 2015

Abstract The interactions between waves, tidal currents, and bathymetry near New River Inlet, NC, USA are investigated to understand the effects on the resulting hydrodynamics and sediment transport. A quasi-3-D nearshore community model, NearCoM-TVD, is used in this integrated observational and modeling study. The model is validated with observations of waves and currents at 30 locations, including in a recently dredged navigation channel and a shallower channel, and on the ebb tidal delta, for a range of flow and offshore wave conditions during May 2012. In the channels, model skills for flow velocity and wave height are high. Near the ebb tidal delta, the model reproduces the observed rapid onshore (offshore) decay of wave heights (current velocities). Model results reveal that this sharp transition coincides with the location of the breaker zone over the ebb tidal delta, which is modulated by semidiurnal tides and by wave intensity. The modulation of wave heights is primarily owing to depth changes rather than direct wave-current interaction. The modeled tidally averaged residual flow patterns show that waves play an important role in generating vortices and landward-directed currents near the inlet entrance. Numerical experiments suggest that these flow patterns are associated with the channel-shoal bathymetry near the inlet, similar to the generation of rip currents. Consistent with other inlet studies, model results suggest that tidal currents drive sediment fluxes in the channels, but that sediment fluxes on the ebb tidal delta are driven primarily by waves.

1. Introduction

Inlet hydrodynamics and sediment transport are critical to many engineering and ecosystem applications such as coastal inundation, dredging, land reclamation, and solute transport. Owing to complex interactions between tidal currents, waves, and bathymetry, extremely heterogeneous and locally intense flows can be generated in an inlet system. Understanding these nonlinear processes and the resulting morphological evolution can be challenging. Through significantly improved remote sensing technology, measurements of the surface flow features and limited information on the bathymetric features can be obtained. However, comprehensive predictions that can provide the information needed for engineering and ecosystem applications still rely on numerical modeling [*Elias et al.*, 2006; *Bertin et al.*, 2009; *Malhadas et al.*, 2009; *Keshtpoor et al.*, 2014]. Thus, one of the goals of this study is to evaluate the predictive skill of an existing wave-averaged quasi-3-D circulation model, NearCoM-TVD [*Shi et al.*, 2003; *Chen et al.*, 2014] for an inlet system under a range of tide and wave conditions.

Many prior studies of the hydrodynamics and morphodynamics of tidal inlets have focused on the mean (tidal) current and the bathymetry [*de Swart and Zimmerman*, 2009]. In the absence of waves, the horizontal pressure gradient and the bottom shear stress are the leading order terms in the momentum balance [*Hench and Luettich*, 2003]. However, waves can dominate inlet processes via wave-breaking and wave-current interaction, including current-induced refraction and Doppler shifts, steepening of waves propagating into opposing currents, and enhanced roughness experienced by currents owing to the wave bottom boundary layer [*Wolf and Prandle*, 1999]. For example, recent field observations at Katama Inlet, MA during Hurricane Irene [*Orescanin et al.*, 2014] and at New River Inlet during Tropical Storm Alberto [*Wargula et al.*, 2014] demonstrate that radiation stress gradients owing to breaking waves can enhance landward-directed flows.

In the past decade, there has been significant improvement in wave-current coupling in wave-averaged coastal modeling systems [*Putrevu and Svendsen*, 1999; *Mellor*, 2005; *Newberger and Allen*, 2007; *Kumar et al.*, 2011]. Using a quasi-3-D circulation model SHORECIRC [*Svendsen et al.*, 2002] coupled with the spectral

© 2015. American Geophysical Union. All Rights Reserved.

wave model SWAN [*Booij et al*., 1999], the ebb tidal shoals at the Golden Gate inlet, CA cause focusing of surface gravity waves [*Shi et al*., 2011]. The resulting gradients in the spatially variable wave-induced setup favor landward-directed flows. The pressure gradient term also was shown to be important in the alongshore momentum balance. Model results from the Regional Ocean Modeling System suggest that wave-driven nearshore circulations are significant and cause alongshore nonuniformity at the inlet and adjacent beach near Willapa Bay, WA (USA) [*Olabarrieta et al*., 2011]. The momentum balance further indicates that during storm conditions, the wave-breaking-induced acceleration is the leading order term balancing the pressure gradient and bottom friction.

To investigate the effects of tidal currents on waves, the steady state wave transformation model STWAVE was coupled with the circulation model ADCIRC [*Smith et al*., 2000]. These simulations suggest that wave heights can be increased up to 80% during the strong (up to 2 m/s) ebb flows that occur in the outer Willapa entrance channel, and can be decreased by 20% during flood. Similarly, wave heights can be increased up to 20% during ebb flows at the mouth of the wave-dominated inlet of Albufeira Lagoon, Portugal owing to current-induced refraction and partial blocking [*Dodet et al*., 2013]. Moreover, the seaward-directed sediment fluxes are attenuated significantly by the effects of wave-current interaction, contributing to the sediment accretion in the inlet [*Dodet et al*., 2013].

A new version of the Nearshore Community Model System, NearCoM-TVD [*Shi et al*., 2003; *Chen et al*., 2014], has been developed to model coastal processes in areas with abrupt changes or discontinuities in bathymetry where conventional finite-difference schemes may produce unphysical oscillations. Specifically, the current version of SHORECIRC was implemented with a hybrid finite-difference finite-volume TVD-type scheme [*Toro*, 2009] that allows for robust treatment of discontinuities. NearCoM-TVD was verified [*Chen et al*., 2014] with a semianalytical solution for an idealized tidal inlet [*Keulegan*, 1967] and with field data over a rip-channel bathymetric system under intense wave-current interaction [*MacMahan et al*., 2010].

Here, a numerical investigation of hydrodynamics and sediment transport at New River Inlet, NC, is carried out using NearCoM-TVD in conjunction with field observations. A brief overview of the model formulation is presented in section 2. The model setup for New River Inlet is discussed in section 3. In section 4, model validation with field-observed significant wave heights and mean velocities is presented, followed by a discussion of the effect of wave-current interaction for a range of tidal forcing and wave intensity. A diagnostic study of residual flow, sediment fluxes, and the resulting morphological change is discussed in section 5.

2. Numerical Model

NearCoM-TVD [*Shi et al*., 2003; *Chen et al*., 2014] couples the spectral wave model SWAN [*Booij et al*., 1999] with the quasi-3-D nearshore circulation model SHORECIRC [*Svendsen et al*., 2002]. SHORECIRC is a two-dimensional horizontal (2DH) model that incorporates the mixing effect induced by the vertical variation of wave-induced horizontal circulation. Similar to most of the river inlet systems in the southern part of North Carolina, fresh water discharge from New River is relatively low [*Pilkey et al*., 1998]. For this well-mixed coastal environment with negligible baroclinic gradients, the present quasi-3-D model is shown to produce results similar to those of fully 3-D circulation models [*Haas and Warner*, 2009]. However, the quasi-3-D model is more computationally efficient than 3-D depth-resolving models, allowing simulations of a large-scale domain (>50 km^2) over monthly timescales with moderate computational effort.

The instantaneous horizontal velocity u_α^{ins} in Cartesian coordinates (x_1, x_2) is split into [*Putrevu and Svendsen*, 1999],

$$u_\alpha^{ins} = u'_\alpha + u_{w\alpha} + u_\alpha + u_{1\alpha} \tag{1}$$

where $\alpha = 1$ is the east-west direction and $\alpha = 2$ is the north-south direction. The components of the instantaneous velocity, u'_α, $u_{w\alpha}$, u_α, and $u_{1\alpha}$ represent the turbulent velocity fluctuations, the wave velocity, the depth-averaged short-wave-averaged velocity, and the vertical variation of the short-wave-averaged velocity, respectively. The depth-averaged short-wave-averaged velocity u_α is defined by "Lagrangian averaging" as

$$u_\alpha = \frac{1}{H}\overline{\int_{-h}^{\zeta} u_\alpha^{ins} dz} \tag{2}$$

where ζ is the instantaneous surface elevation and the total water depth H= $\eta+h$, in which h is the still water level and η is the wave-averaged surface elevation.

A coordinate transformation is performed between the Cartesian coordinates x_α and the generalized curvilinear coordinates ξ^α, and thus the contravariant components of the velocity vector can be expressed by

$$u^\alpha = u_\beta \frac{\partial \xi^\alpha}{\partial x_\beta} \tag{3}$$

where the superscript $(\ )^\alpha$ represents the contravariant component of a vector, and subscript $(\ )_\alpha$ is the Cartesian component of a vector. To use the TVD numerical scheme, the conservative form of the SHORECIRC equations can be written in generalized curvilinear coordinates as [*Chen et al*., 2014],

$$\frac{\partial \eta}{\partial t} + \frac{1}{J}\frac{\partial JP^\alpha}{\partial \xi^\alpha} = 0 \tag{4}$$

$$\begin{aligned} &\frac{\partial Hu_\infty}{\partial t} + \frac{1}{J}\frac{\partial}{\partial \xi^\beta}\left[JP^\beta u_\alpha + \frac{1}{2}g\left(\eta^2+2\eta h\right)J\frac{\partial \xi^\alpha}{\partial x^\beta}\right] + f_\alpha \\ &-g\eta\frac{1}{J}\frac{\partial}{\partial \xi^\beta}\left(hJ\frac{\partial \xi^\alpha}{\partial x^\beta}\right) + \frac{1}{\rho J}\frac{\partial}{\partial \xi^\gamma}\left(S_{\alpha\beta}J\frac{\partial \xi^\gamma}{\partial x^\beta}\right) \\ &+\frac{1}{J}\frac{\partial}{\partial \xi^\gamma}\left(\tau_{\alpha\beta}J\frac{\partial \xi^\gamma}{\partial x^\beta}\right) + \frac{\tau_\alpha^b}{\rho} - \frac{\tau_\alpha^s}{\rho} + ROT = 0 \end{aligned} \tag{5}$$

where J is the Jacobian determinant, and $P^\alpha = Hu^\alpha$ denotes the contravariant component of volume flux. In equation (5), all vector forcing terms are in Cartesian coordinates so there is no need to make a transformation for the second-order tensor. The Cartesian components of the Coriolis force f_α are $-f_c Hu_2$ and $-f_c Hu_1$, where f_c is the Coriolis coefficient, u_2 is the north-south velocity, and u_1 is the east-west velocity. $S_{\alpha\beta}$ is the Cartesian component of radiation stress [*Longuet-Higgins and Stewart*, 1962, 1964], τ_α^b is the Cartesian component of bottom stress, τ_α^S is wind stress [*Van Dorn*, 1953], and *ROT* represents the remaining terms associated with diffusion, atmospheric pressure, and 3-D dispersion [*Shi et al*., 2003].

To the lowest order, the equation governing the vertical structure of horizontal velocity is

$$\frac{\partial u_{1\alpha}^{(0)}}{\partial t} - \frac{\partial}{\partial z}\left(\upsilon_t \frac{\partial u_{1\alpha}^{(0)}}{\partial z}\right) = F_\alpha \tag{6}$$

where υ_t is the eddy viscosity and F_α is a general form of the local forcing [see *Putrevu and Svendsen*, 1999, equation (31) for more details]. The solution of depth variant current velocity $u_{1\alpha}$ is the same as that discussed previously [*Shi et al*., 2003]. The bottom current velocity u_α^b can be evaluated using u_α and $u_{1\alpha}$ at $z=-h$

$$u_\alpha^b = u_\alpha + u_{1\alpha}(z=-h) \tag{7}$$

The bottom friction can be altered by the local water depth, grain-related roughness, and apparent roughness resulting from wave-current interaction. For example, the bottom friction is enhanced by wave-current interactions owing to bottom boundary layer processes, and is not simply a linear sum of the wave-induced and current-induced friction. Incorporating the enhancement of the bottom friction by nonlinear wave-current interactions is essential for simulating the observed flow field in the frontal region at New River Inlet [*Rogowski et al*., 2014]. Many theories and models have been proposed to describe the nonlinear behavior of wave-current interaction [*Grant and Madsen*, 1979]. For computational efficiency, a data-based method [*Soulsby*, 1997] is applied. The bottom friction under the interaction of currents and waves can be estimated by

$$\tau_\alpha^b = y(\tau_\alpha^c + \tau_\alpha^w) \tag{8}$$

where τ_α^c is the current-only bottom stress, τ_α^w is the wave-only bottom stress, and

$$y = x\left[1 + bx^p(1-x)^q\right] \tag{9}$$

with

$$x=\tau_\alpha^c/(\tau_\alpha^c+\tau_\alpha^w) \tag{10}$$

and

$$b=(b_1+b_2|cos\ \phi|^{8.8})+(b_3-b_4\ |cos\ \phi|^{8.8})\log_{10}(\frac{f_w}{C_D}) \tag{11}$$

where f_w is the friction factor used to compute τ_α^w, and C_D is the friction factor used to compute τ_α^c. The bottom friction f_w is calculated from an explicit formula [*Swart*, 1974], and C_D can be obtained from the logarithmic velocity profile with a given roughness length z_o, here assumed to be $z_o=0.001$ m. The fitting coefficients b_1, b_2, b_3, and b_4 and the coefficients of the analogous expressions for p and q can be found in *Soulsby et al*. [1993] and *Soulsby* [1997].

The total load (bedload plus suspended load) sediment transport formula [*Soulsby*, 1997] in the existing NearCoM-TVD sediment transport module can be written as

$$q_t=A_s|u|\left[(|u|^2+\frac{0.018}{C_D}u_{rms}^2)^{1/2}-u^{cr}\right]^{2.4}(1-1.6tan\beta) \tag{12}$$

where $|u|$ is the magnitude of the current velocity, u_{rms} is the root-mean-square wave orbital velocity, u^{cr} is the threshold current velocity of sediment motion [*van Rijn*, 1984], β is the bed slope, and A_s is a coefficient associated with bedload and suspended load.

3. Model Setup of New River Inlet, NC

New River Inlet (NRI) (Figure 1) is located on the southeast coast of North Carolina. The NRI system consists of a large backbay area (approximately 68 km^2), a relatively narrow (~200 m wide), and shallow (~3 m depth) inlet connecting to the Atlantic Ocean, and an ebb tidal delta offshore of the inlet mouth [*MacMahan et al*., 2014]. The system (including the inlet and ebb shoal) includes a channel ($3<$ depth <10 m, recently dredged across the ebb delta to 2 m below ambient sand level) on the southwestern side and a shallower channel (depth ≤ 3 m) on the northeastern side (Figure 1b). An array of colocated pressure gauges and current meters was deployed during May 2012 along the channels, across the ebb tidal delta ($<$ 2m water depth), and around the offshore edge of the ebb shoal (Figure 1b).

The model domain (dashed box in Figure 1a) includes the inlet channels, the surf zone, the continental shelf, and the large lagoon behind the inlet. The digital elevation model (DEM), which has vertical data on a 10 m grid based on the North American Vertical Datum 88 (NAVD 88) standard, is comprised of three data sets: the DEM of Onslow Beach and the Intracoastal waterway (ICW) from USACE LARC bathymetry (November, 2005) and VIMS Swath bathymetry (August 2008), the DEM in New River Estuary from USACE Swath bathymetry (August 2009), and the DEM (Figure 1b) surveyed on 1 May 2012 by USACE covering the inlet and the ebb tidal delta. These three DEMs are integrated to provide the bathymetry used here. The 10 m resolution DEM is interpolated into a curvilinear mesh with the highest resolution of 10 m at the inlet. In the offshore and backbay areas, the mesh size is increased to about 200 m. There are 108,800 grid points in the computational domain. Modeled circulation patterns and significant wave heights from a grid convergence test using a minimum grid size of 5 m near the inlet and the surf zone are consistent with those from the 10 m resolution model, suggesting that the main findings are robust. The model results are compared with observations from wave buoys and bottom-mounted colocated pressure gauges and current meters for a one-month period (May 2012). To compare with model results, the measured current profiles at sensors 0–9 (see Figure 1b for sensor locations) are depth averaged. The current velocities at other locations (Figure 1b) were measured approximately 0.8 m above the seafloor. The estimated distance above the seafloor does not account for the erosion and accretion (typically less than 0.2 m) during the study.

The spatially varying phases and amplitudes of the M2, S2, N2, K2, O1, and K1 tidal constituents provided by the ADCIRC [*Luettich et al*., 1992] database are applied at the southwest, southeast, and northeast open boundaries of the circulation model SHORECIRC (Figure 1a). The dominant tidal constituent is M2 (tidal amplitude ~0.63 m), with smaller amplitudes at other tidal constituents, including K1 (amplitude ~0.11 m), S2 (amplitude ~0.08 m), and O1 (amplitude ~0.08 m) [*MacMahan et al*., 2014]. The boundary conditions include two spring tides and one neap tide (Figure 2a). The boundaries adjacent to the lagoons and the

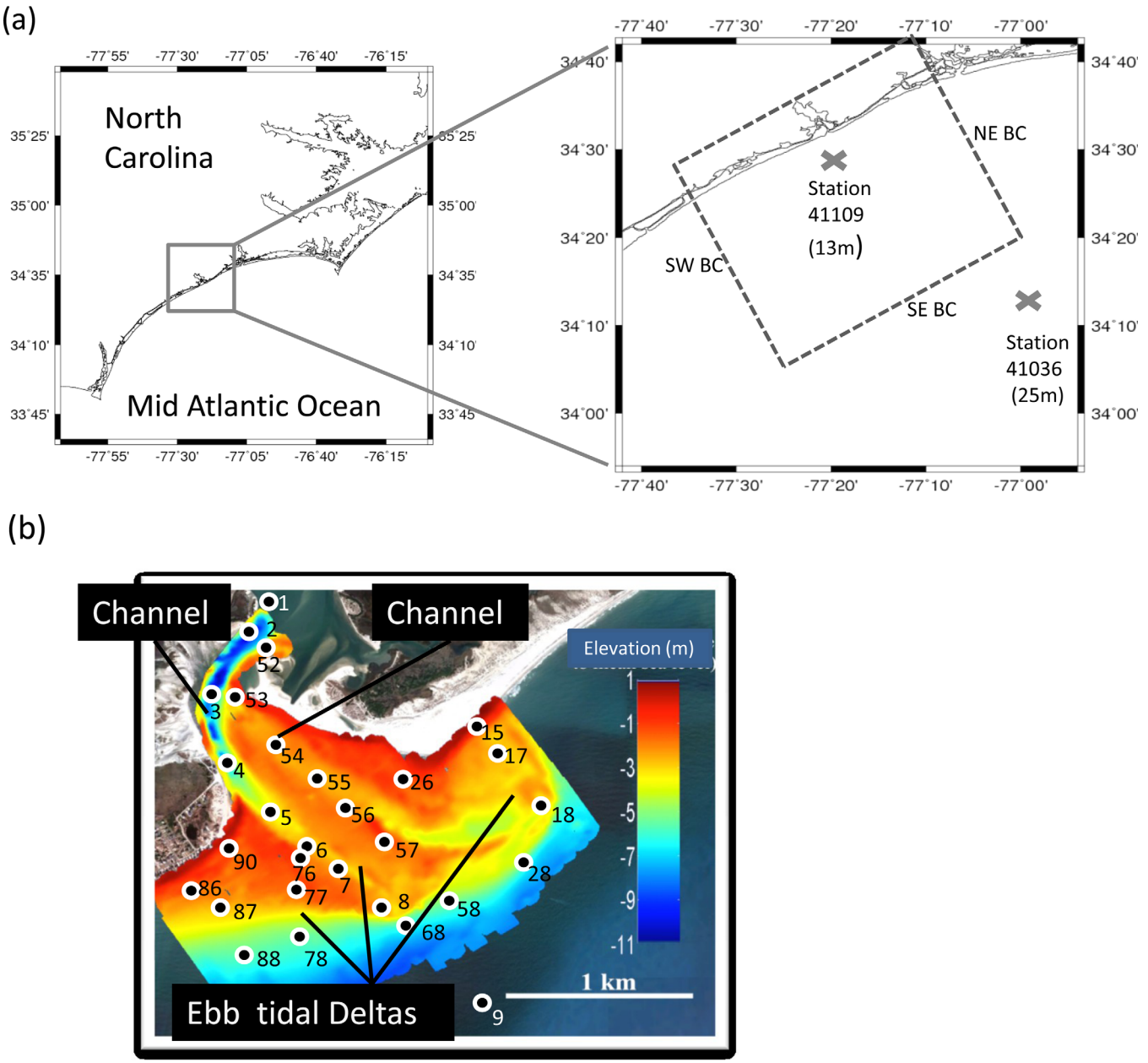

Figure 1. (a) Location and configuration of New River Inlet, NC: the dashed box is the computational domain and the cross symbols are NOAA buoys. The tidal constituents provided by the ADCIRC [*Luettich et al.*, 1992] database are applied at the southwestern, southeastern, and northeastern open boundaries of the circulation model SHORECIRC. (b) An expanded view of the inlet entrance with colocated pressure gauges and current meters (circles) and bathymetry (color contours, scale on the right) superposed on a Google Earth image.

backbay area are closed. The significant wave height and peak period observed at NOAA station 41036 (25 m depth, see Figures 2b and 2c, also see Figure 1a for the location) are applied to the southeast boundary of the spectral wave model SWAN. The mean wave direction estimated with observations at NOAA station 41109 (13 m depth, see Figure 2d, also see Figure 1a for the location) is used instead of the directions at NOAA station 41036 because there was no directional information for about 37% of the observations in 25 m depth. The observed wave heights ranged from 0.5 to 3.1 m and the incident waves usually were from the southeast (near normally incident). Wind speed and direction measured near the inlet mouth also are used in the circulation and spectral wave models. The Coriolis parameter is calculated using the latitude of New River Inlet (34.10N).

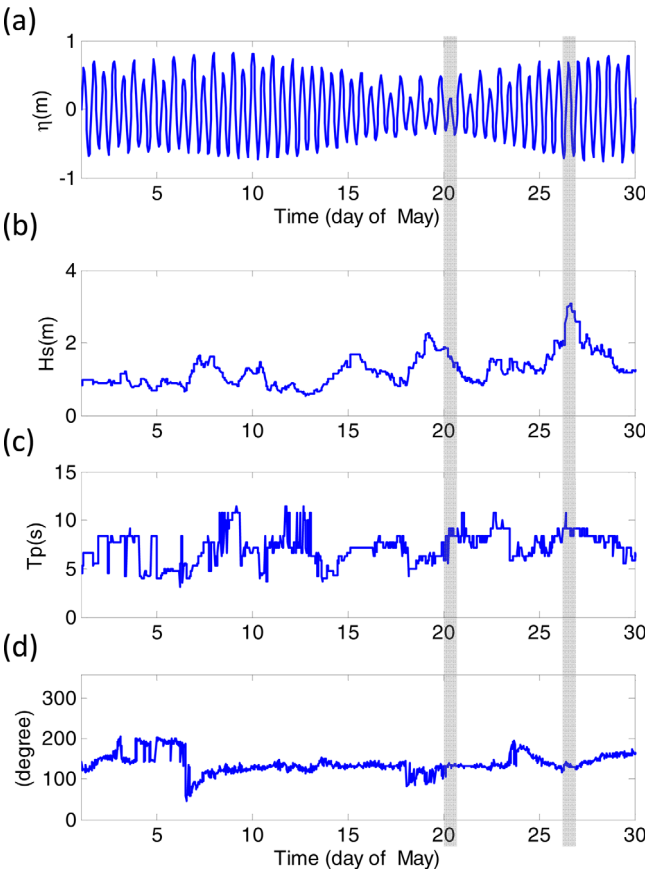

Figure 2. (a) Sea-surface elevation boundary condition provided by the ADCIRC tidal database and (b) significant wave heights, (c) peak periods observed at NOAA station 41036 (25 m depth, Figure 1a), and (d) wave direction observed by NOAA station 41109 (13 m depth, Figure 1a) versus time. The 13 m depth directions are used because there was no directional information for 37% of the observations in 25 m depth. Two scenarios (spring and neap tide conditions) indicated by the gray bars are discussed in section 4.

4. Model Results

Snapshots of model results on 27 May during a spring tide (tidal amplitude 0.7 m) with energetic waves (offshore (25 m depth) significant wave height of 3.1 m from tropical storm Alberto, Figure 2) illustrate the flood-ebb flow patterns (Figure 3). During the maximum flood (13:00 h EDT, Figure 3a), flow is funneled into the inlet owing to the water level difference between the inlet and the open sea. Peak flow velocities in the deeper (southwestern) channel are predicted to exceed 1.5 m/s, while peak flow velocity on the southwest side of the ebb tidal delta is ∼0.4 m/s. During the maximum ebb (19:00 pm EDT, Figure 3b), the instantaneous model flow field shows the characteristics of an ebb tidal jet with flow intensity usually larger in the channels ($>$ 1.5 m/s) than over the shoals ($<$ 0.5 m/s). The ebb jet splits into two near the inlet entrance where the deeper and the shallower channels are separated by the center section of the ebb tidal delta. The jet near the southwestern side of the inlet is stronger and wider than the jet in the northeast. During maximum ebb flow, the southwestern jet can penetrate through the surf zone and into deep water (exceeds 8 m depth, Figure 3b). Slightly south and west of the jet, the modeled ebb flow intensity attenuates rapidly near the outer edge of the ebb tidal delta. The weaker ebb tidal jet in the shallower channel to the northeast is diverted northeastward in the alongshore direction. The model predicts eddy-like circulation patterns just off the northeastern shore and on the southwest side of the ebb tidal delta (indicated by the boxes in Figures 3a and 3b).

The wave field near the inlet is modulated significantly by the tides. During maximum flood (Figure 3c), waves are predicted to break over the ebb tidal delta where the local water depth is less than 2 m and the peak wave height exceeds 0.6 m. However, waves can penetrate into the inlet, and a significant wave height of 0.3–0.5 m is predicted slightly landward of the entrance. During maximum ebb flow (Figure 3d), waves break in a narrow region at the outer edge (2 m depth) of the ebb tidal delta. The modeled wave height decreases across the width of the ebb shoal to about 0.1–0.2 m at the inlet entrance. Modeled wave heights are consistent with the observations (compare colors within the small circles (observations) in Figures 3c and 3d with nearby color contours (model)). Although model skill typically is high, wave height is overpredicted at sensor 15 (Figures 3c and 3d, sensor 15 is close to shore, northeast of the inlet channels), possibly owing to its shallow depth, and wave height is underpredicted during flood at sensors 3 and 53 in the inner part of the inlet channel (Figure 3c). The hydrodynamics at this inlet system are complex owing to the interactions between tidal currents, waves, and local bathymetry. A more thorough discussion of the model performance is given next.

4.1. Model Performance

The model accuracy is assessed with the Wilmott Skill score [*Willmott*, 2005], defined as

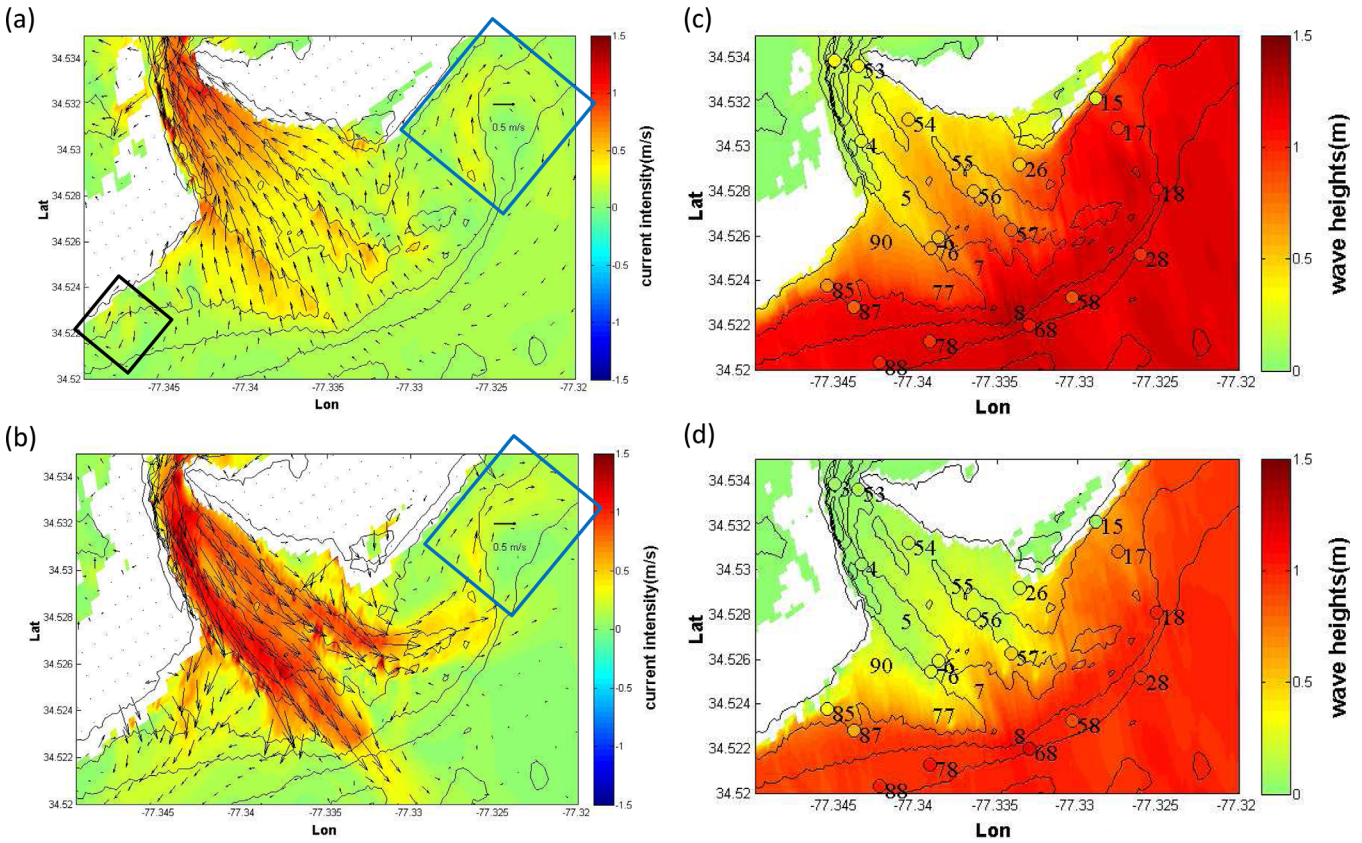

Figure 3. The modeled instantaneous flow field (vectors indicate direction and color contours indicate current intensity, scale on the right) during (a) maximum flood and (b) maximum ebb on 27 May, a spring tide-stormy wave condition. The boxed areas in Figures 3a and 3b surround circulation patterns discussed in the text. Modeled (color contours) and observed (colors inside the small circles at sensor locations) wave heights during (c) maximum flood and (d) maximum ebb. If the model and data are the same, the circle color equals the nearby color contour. The solid curves are bathymetric contours (0, 2, 4, 6, and 8 m depth relative to NAVD88).

$$\chi = 1 - \frac{\sum_{i=1}^{N} |X_{mod} - X_{obs}|^2}{\sum_{i=1}^{N} \left(|X_{mod} - \bar{X}_{obs}| + |X_{obs} - \bar{X}_{obs}| \right)^2} \tag{13}$$

where N is the sample size, X is the variable being compared, $\bar{X}$ is the sample mean, and the subscript $(\,)_{mod}$ and $(\,)_{obs}$ represent the modeled and observed values, respectively. The skill value χ is between 0 (no agreement) and 1 (perfect agreement). The skill values of predicted significant wave heights and current velocities are summarized in Table 1. The lowest skill values (< 0.5) usually occur at locations where the observed wave heights or velocities were small (Table 1, root mean square (RMS) values of measured wave heights and velocities). Additional model-data comparisons and plan view maps of model skill are presented elsewhere [*Chen et al*., 2014].

The model accurately predicts the significant wave heights, peak periods, and directions measured in 13 m depth at NOAA station 41109 (Figures 4a–4c) (χ=0.89 for wave height, χ=0.75 for peak period, and χ=0.86 for wave direction). Wave heights in 9 m depth (sensor 9) also are predicted well (Figure 4d, χ=0.87), suggesting that the modeled wave field seaward of the ebb tidal delta is accurate. At sensor 68 (5 m depth), onshore of sensor 9 (Figure 1b), the modeled phase and magnitude of tidal surface elevation is accurate (Figure 4e, $\chi = 0.95$).

The numerical model skillfully predicts the observed significant wave heights at most locations in the channels and on the ebb deltas (Table 1; skill values typically are greater than 0.7). The model skill is slightly lower at sensor 68 ($\chi = 0.59$) in the outer surf zone where refraction is large and the tidal jet intensity diminishes rapidly (discussed further below). Model skill is lower around the bend in the inlet channel at sensor 3

Table 1. Model Skill of Wave Heights, East-West Velocity (u), North-South Velocity (v) and Magnitude of Velocity (Speed) for All the Sensors, and RMS Values of Observed Wave Heights and Velocities

	Model Skill χ				RMS Value		
Sensor Number	H_s	u	v	Flow Speed	H_s (m)	u (m/s)	v (m/s)
0	0.14	0.89	0.93	0.73	0.02	0.19	0.55
1	0.26	0.85	0.84	0.61	0.02	0.18	0.43
2	0.16	0.83	0.86	0.57	0.05	0.36	0.46
3	0.60	0.48	0.92	0.62	0.20	0.17	0.49
4	0.73	0.80	0.85	0.57	0.14	0.30	0.73
5	0.87	0.96	0.95	0.87	0.23	0.27	0.48
6	0.75	0.92	0.91	0.86	0.33	0.25	0.44
7	N/A	0.46	0.48	0.40	N/A	0.12	0.15
8	N/A	0.62	0.83	0.73	N/A	0.16	0.26
9	0.87	0.38	0.20	0.31	0.77	0.08	0.05
15	0.70	0.39	0.47	0.41	0.44	0.16	0.10
17	0.84	N/A	N/A	N/A	0.57	N/A	N/A
18	0.91	N/A	N/A	N/A	0.77	N/A	N/A
26	0.71	0.90	0.75	0.61	0.32	0.25	0.19
28	0.71	0.64	0.50	0.50	0.63	0.05	0.05
52	0.41	0.68	0.23	0.50	0.02	0.34	0.03
53	0.65	0.78	0.69	0.55	0.20	0.16	0.54
54	0.82	0.92	0.87	0.64	0.26	0.25	0.49
55	0.87	0.95	0.93	0.85	0.28	0.27	0.34
56	0.82	0.93	0.93	0.86	0.33	0.26	0.24
57	0.76	0.69	0.50	0.45	0.50	0.16	0.14
58	0.70	0.55	0.43	0.47	0.55	0.12	0.05
68	0.59	0.64	0.42	0.52	0.51	0.07	0.06
76	0.82	0.85	0.88	0.85	0.39	0.19	0.53
77	0.77	0.67	0.86	0.57	0.42	0.13	0.21
78	0.76	0.45	0.66	0.42	0.69	0.03	0.04
85	0.70	0.49	0.60	0.43	0.47	0.25	0.13
87	0.87	0.61	0.73	0.73	0.65	0.27	0.10
88	0.77	0.58	0.64	0.38	0.69	0.05	0.04
90	0.84	0.74	0.80	0.51	0.38	0.11	0.32

($\chi = 0.60$) and 52 ($\chi = 0.41$), and skill becomes poor at sensors farther shoreward where observed wave heights are small (< 0.1 m).

In the southwestern (deeper) channel (sensors 1–6), the model skill for velocity is high (Table 1). For example, at sensor 5, east-west flows are predicted well, and although north-south flows are slightly underpredicted, the overall agreement is excellent (Figures 5a and 5b, $\chi > 0.9$). The modeled tidal flows and water-depth changes modulate the wave heights, consistent with the observations (Figure 5c). Tidal flows at NRI are progressive, and thus, peak flood and ebb coincide with high and low tide, respectively [*Wargula et al.*, 2014]. Model skill also is high in the northeastern (shallower) channel (Table 1, e.g., $\chi > 0.6$ at sensors 53–56).

Model skill is lower near the bend in the channel (sensors 3 and 52), possibly owing to veering flow directions, to the importance of vertical structure and lateral flows that are neglected in the depth-averaged model [*Nidzieko and Ralston*, 2011], or to uncertainties in the bathymetry. In particular, the bathymetry of the flood tidal deltas was not surveyed (the area between sensors 52 and 53, Figure 1b). The modeled velocities also are less accurate near the offshore edge of the ebb shoal, where the ebb tidal jet diminishes sharply, flows are relatively weak (RMS magnitudes < 0.16 m/s, Table 1), and waves start to dominate (see Table 1, sensors 9, 88, 78, 68, 58, 7, 57, and 28). For example, at sensor 58, the observed and predicted tidal flows have become weak (compare Figures 6a and 6b with Figures 5a and 5b), and wave heights are larger and less dominated by the tides than at sensor 05 (compare Figure 6c with Figure 5c). Although the model slightly overpredicts the significant wave height at sensor 58, the temporal evolution is modeled well (Figure 6c). The flows near the beach alongshore of the inlet (sensors 15 and 85), which sometimes are driven by breaking waves and sometimes by tidal flows, also are difficult to model. Comparisons of model simulations with and without wind forcing suggest wind-driven flows are small (not shown).

A narrow transition region between tidal-current-dominant and wave-dominant conditions is observed and predicted on the southwestern ebb delta (Figure 7). In particular, wave heights vary over multiday periods at sensor 78 (Figure 7a, sensor 78 is in 5 m water depth, offshore of the southwest side of the ebb delta,

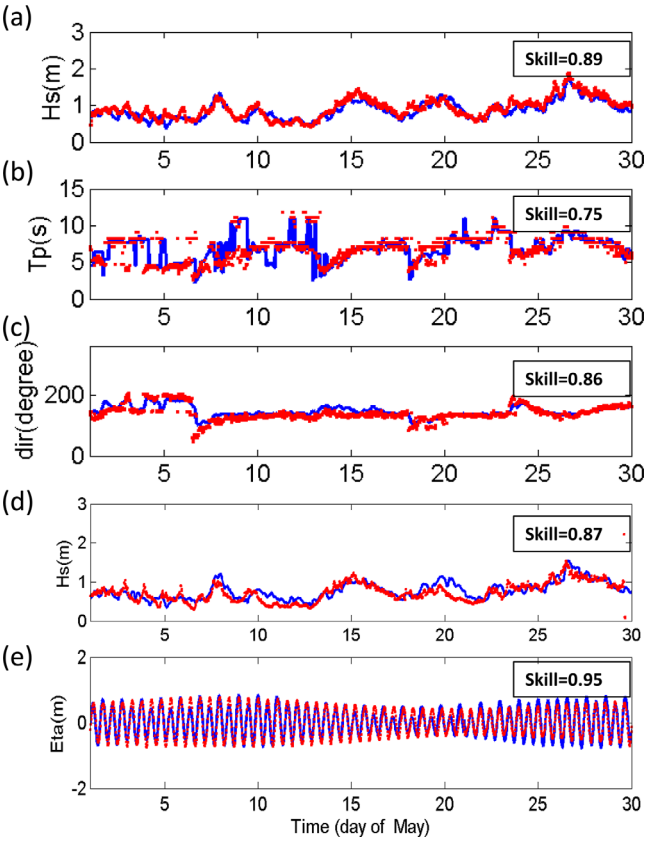

Figure 4. Modeled (blue curves) and measured (red dots) (a) significant wave height, (b) peak period, and (c) wave direction in 13 m depth (NOAA station 41109,Figure 1a) and (d) significant wave height and (e) sea-surface elevation in 9 m depth (sensor 68, Figure 1b) versus time.

Figure 1b) in response to offshore winds, but only a few hundred meters onshore, wave heights are relatively small and tidally modulated (sensors 76 and 77, Figures 7a–7c). Flow speeds are small at sensor 78 (RMS speed $\sim$ 0.05 m/s), but become large and tidally modulated at sensor 76 (Figures 7d–7f). The model-data discrepancies in current speeds between 5th and 10th May and between 15th and 25th May at sensor 76 may be owing to the effects of subtidal motions [*MacMahan et al.*, 2014] or freshwater discharge [*Rogowski et al.*, 2014], which are not included in the model boundary condition. Comparisons of model simulations with and without the mixing term suggest that the tidally dominated flows near the inlet mouth are not sensitive to the mixing induced by vertical variations of horizontal currents, which can be important for wave-driven flows inside the surfzone. Thus, the quasi-3-D simulations are similar to those from a conventional depth-averaged approach. Although skill is only fair at some locations in this complicated region, the model simulates the dynamics of the inlet, and in particular reproduces the wave and current patterns of the sharp transition, which is discussed further in section 5.

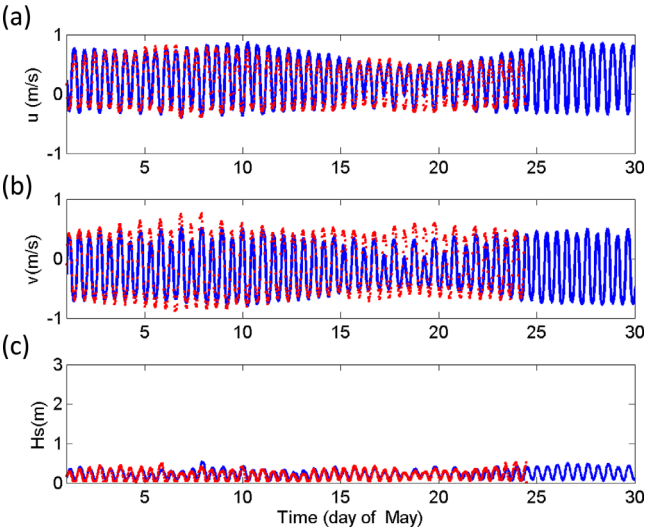

Figure 5. Modeled (blue curves) and measured (red dots) (a) east-west (u) velocity, (b) north-south (v) velocity, and (c) significant wave height (H_s) at sensor 05 in the southwestern channel (Figure 1b) versus time.

4.2. Wave-Current Interaction in Different Scenarios

The validated numerical model is used to investigate the nearshore circulation patterns and the role of wave-current interaction. In particular, to investigate the effect of waves, the model is run with the May 27 tides, but with an offshore significant wave height of only 1 m to simulate a spring tide-mild wave condition (Figures 8a and 8b). Consistent with field observations [*Wargula et al.*, 2014], the model results suggest that flood velocities are stronger throughout the ebb tidal delta when waves are more energetic (compare Figure 8a with Figure 3a). In particular, the flood velocities are increased by 50–100% on the ebb tidal delta when the offshore significant wave height increases from 1.0 to

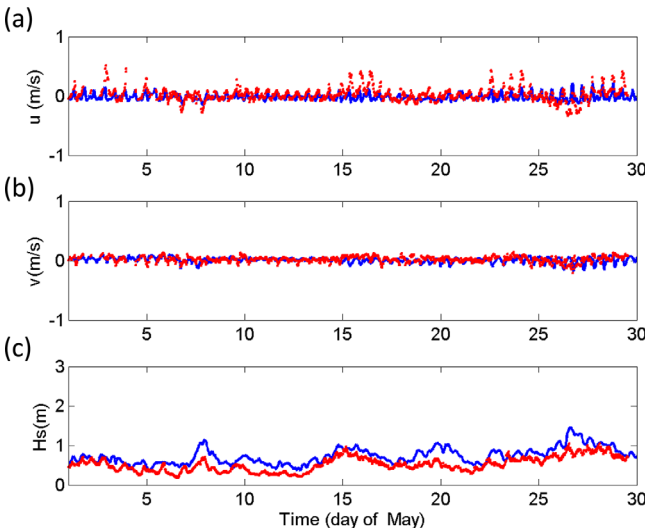

Figure 6. Modeled (blue curves) and measured (red dots) (a) east-west (u) velocity, (b) north-south (v) velocity, and (c) significant wave height (H_s) at sensor 58 on the outer edge of the ebb tidal delta (Figure 1b) versus time.

3.1 m. In addition, for smaller waves, the eddy-like circulation patterns on the northeastern and southwestern sides of the ebb tidal delta are weaker than they are for larger waves (compare circulation patterns in Figure 8a with those in the boxes in Figure 3a). During the maximum ebb, the predicted flow fields for large and small waves are similar (compare Figure 8b with 3b), suggesting that the flow field during spring-tide maximum ebb is dominated by tides.

To determine if the tidal modulation of wave heights primarily is owing to depth changes or to direct interactions with the tidal current, a numerical experiment was conducted with the tidal current and wave forcing of the spring tide-mild wave condition, but without depth changes (Figures 9a and 9b). When depth changes are neglected, the wave field predicted for flood is similar to that for ebb (compare Figures 9a with 9b, and with Figures 8a and 8d, which include the depth changes). Thus, the model results suggest that the wave height modulation is mainly caused by tidal depth changes, not by wave-current interaction, consistent with prior model results at Willapa Bay [*Olabarrieta et al.*, 2011].

During the neap tide-moderate wave conditions on 20 May (tidal amplitude of 0.5 m, offshore significant wave height of 2 m), the modeled flow intensity near the inlet entrance during maximum flood is less than 0.3 m/s in the channels, but more than 0.5 m/s on the ebb tidal delta (Figure 10a). This enhancement of flows over the shoals is different from that predicted during the spring tide conditions (Figure 8a). Furthermore, clockwise circulation patterns can be observed near the entrances of the two channels (black boxes in Figure 10a). During maximum ebb, the tidal jet is weaker during neap tides (Figure 10b) than during spring tides (Figure 8b), as expected. Meanwhile, the alongshore current and clockwise circulations at the northeastern shore during maximum ebb flow are more intense with larger waves (Figure 8b) than with smaller waves (blue box in Figure 10b). This strength of the clock-wise circulation pattern appears to be associated with the wave energy (discussed further in section 5.2).

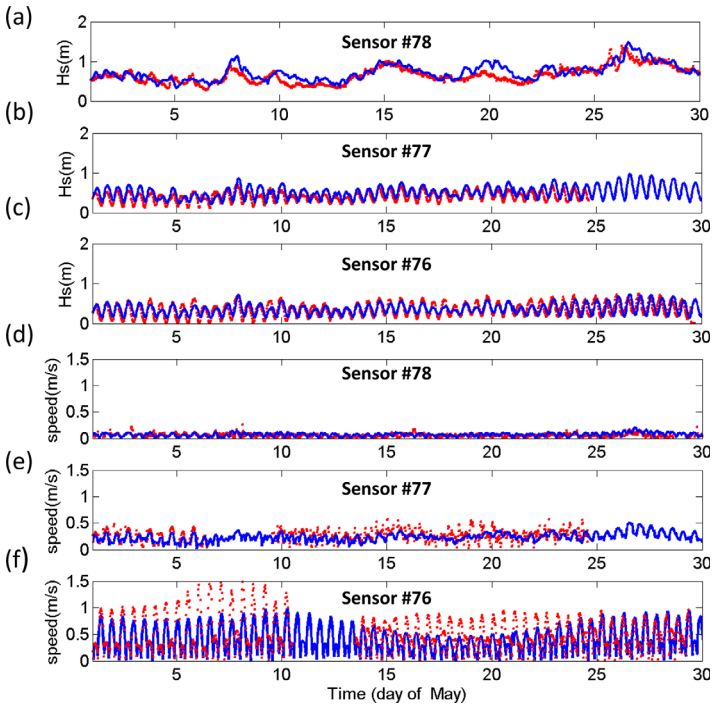

Figure 7. Modeled (blue curves) and measured (red dots) (a, b, and c) significant wave height and (d, e, and f) current speed at sensors 78, 77, and 76 versus time.

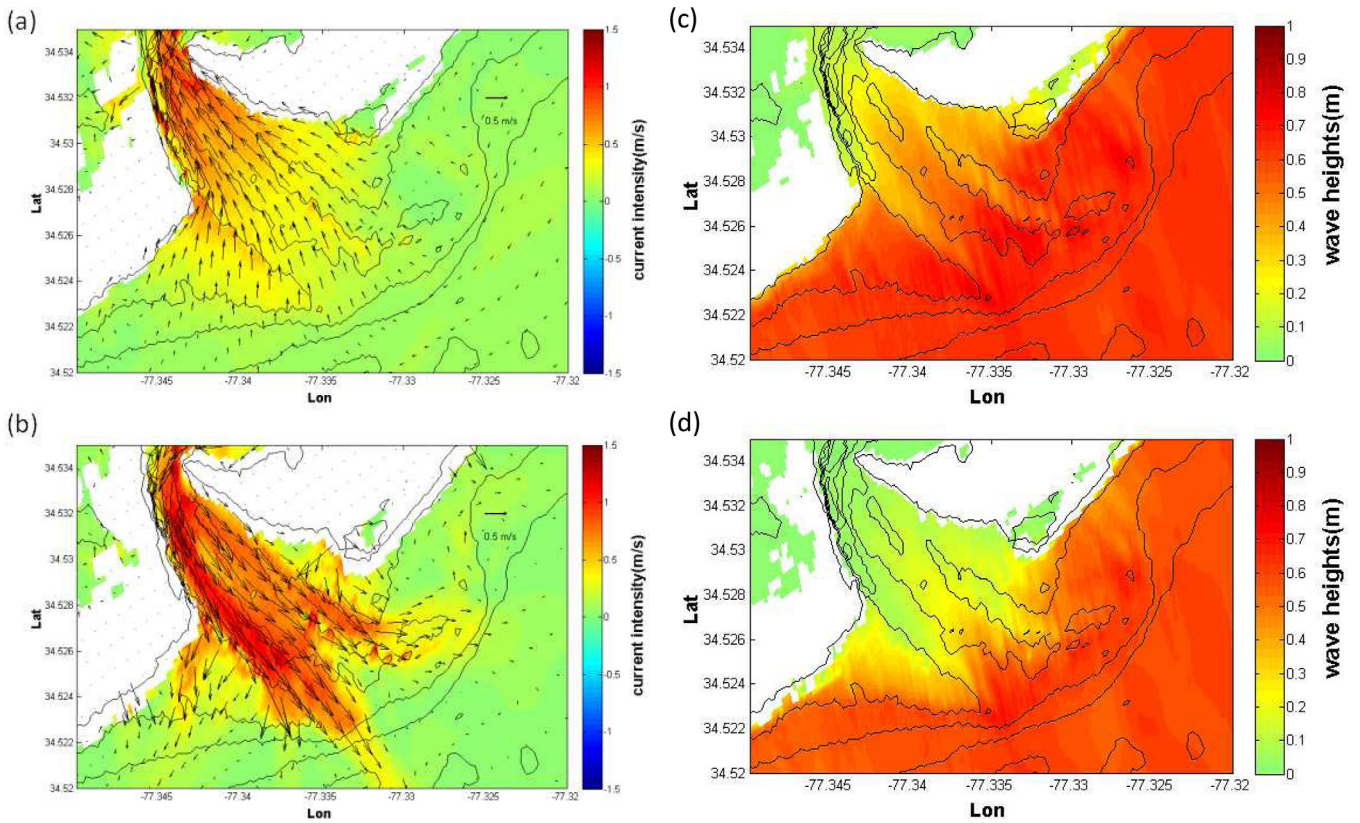

Figure 8. The modeled instantaneous flow field (vectors indicate direction and color contours indicate current intensity, scale on the right) during (a) maximum flood and (b) maximum ebb for a spring tide-mild wave condition (tides are identical to that of 27 May, but with smaller significant wave height) Modeled (color contours) wave heights during (c) maximum flood and (d) maximum ebb. The solid curves are bathymetric contours (0, 2, 4, 6, and 8 m depth relative to NAVD88).

Thus, model results suggest that although the system is tidally dominated in the channels, wave-induced circulations, and alongshore currents prevail on the ebb tidal delta and in the nearshore region on both sides of the entrance. In the nearshore region away from the inlet, wave-induced circulation patterns often are driven by the interaction between waves and bathymetry [*MacMahan et al*., 2006 and reference therein]. The interaction between tidal jets, waves, and bathymetry near the inlet is clarified further in section 5.2.

5. Discussion

5.1. A Sharp Transition Through the Breaker Zone

A sharp transition between wave-dominated and (tidal) current-dominated hydrodynamics is observed and predicted across the southwest side of the ebb tidal delta (sensors 78, 77, 76, Figure 7). This sharp transition of wave and current patterns has important implications for nearshore mixing and sediment transport. The rate of wave energy dissipation associated with breaking is used to illustrate the mechanisms controlling this phenomenon. Around the southwest side of the ebb tidal delta during high tide (maximum flood) the rate of energy dissipation is highest (red contours in Figure 11a) along the shoreline and at the onshore edge of the ebb tidal delta (between sensors 76 and 77, near the edge of the newly dredged channel). The rate of energy dissipation is much weaker (orange and yellow contours, Figure 11a) over the outer (offshore) ebb tidal delta. Thus, the model suggests that there is occasional wave breaking and weak spilling across the entire ebb tidal delta at high tide. In contrast, during low tide (maximum ebb), large dissipation rates occur along the 2 m depth contour on the outer edge of the southwestern ebb tidal (between sensors 77 and 78), as well as near the newly dredged channel (Figure 11b). The model suggests that the location of the breaker zone, and the total wave dissipation across the southwestern delta, are modulated by the tidally varying water depth (compare Figure 11a with Figure 11b).

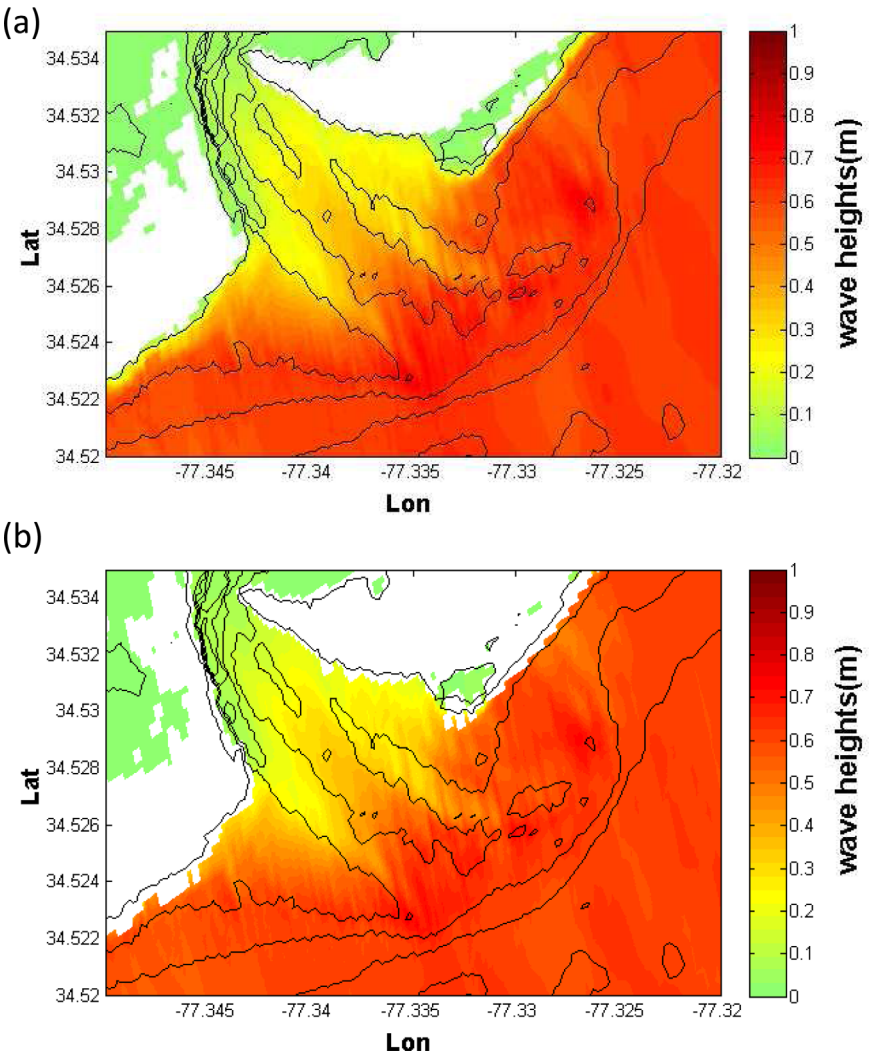

Figure 9. Modeled wave heights during (a) maximum flood and (b) maximum ebb without the effect of depth changes for a spring-tide mild-wave condition (see Figure 8). The solid curves are bathymetric contours (0, 2, 4, 6, and 8 m depth relative to NAVD88).

5.2. Tidally Averaged Residual Flow Velocities: The Effect of Wave-Current Interaction

The snapshots of maximum flood and ebb flows (high and low tide) show persistent circulation patterns, especially during more energetic wave conditions (Figures 3 and 10). Here, the tidally averaged, or residual, flow fields that are important to mixing and transport in coastal systems [*Longuet-Higgins*, 1969; *Uncles and Jordan*, 1980] are examined using M2 tidal forcing. Thus, the simulations are used as a diagnostic tool to investigate the persistent circulation pattern qualitatively, but not to represent realistic subtidal flow patterns.

The tidally averaged velocity can be obtained directly by time averaging the flow velocity vector over a tidal cycle:

$$\mathbf{U}_{r1} = \langle \mathbf{u} \rangle \tag{14}$$

where "$< >$" represents time-average over a tidal cycle. The residual flow, $\mathbf{U}_{r1}$, commonly known as the Eulerian-averaged residual flow, is useful for evaluating possible sediment transport and bottom stress patterns [*Soulsby*, 1997]. Alternatively, the tidally averaged velocity could be obtained from tidally averaged mass fluxes normalized by the averaged flow depths:

$$\mathbf{U}_{r2} = \langle \mathbf{u}H \rangle / \langle H \rangle \tag{15}$$

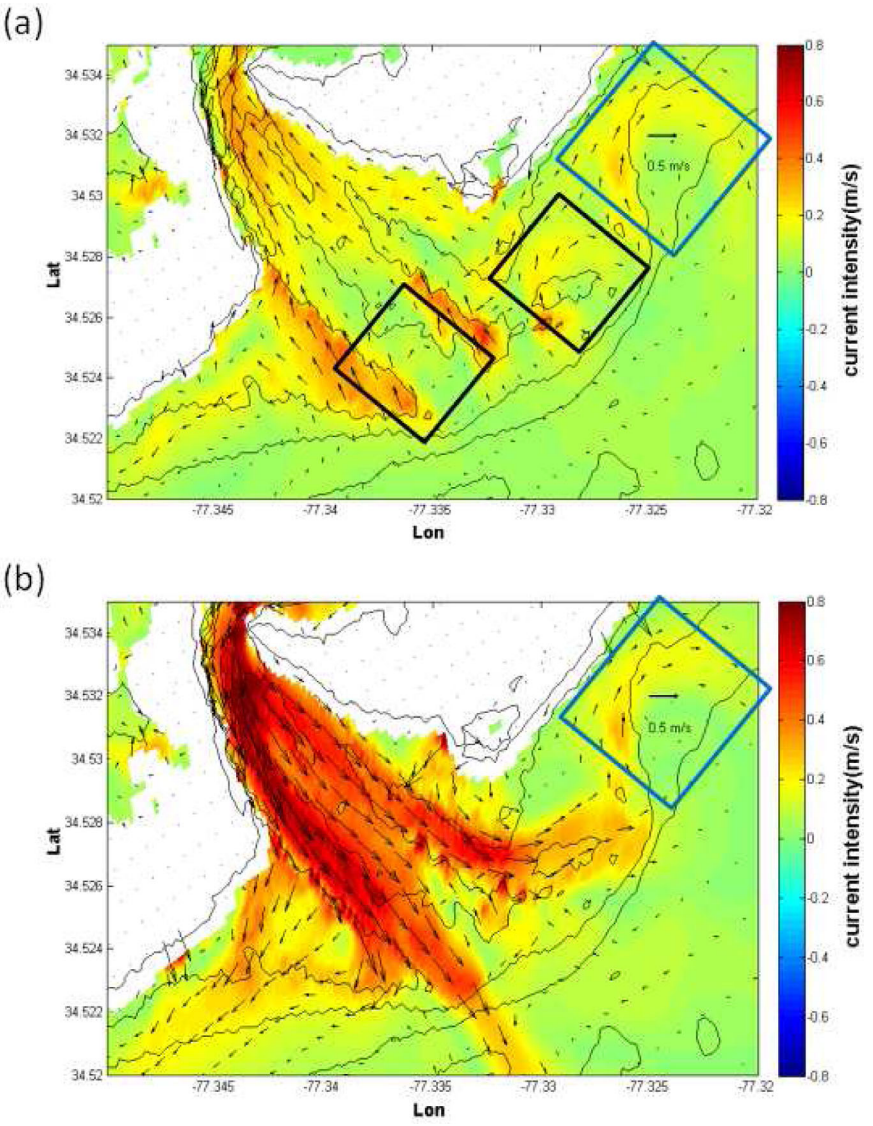

Figure 10. The modeled instantaneous flow field (vectors indicate direction and color contours indicate current intensity, scale on the right) during (a) maximum flood and (b) maximum ebb on 20 May (a neap tide-moderate wave condition. The solid curves are bathymetric contours (0, 2, 4, 6, and 8 m depth relative to NAVD88). The boxed areas surround circulation patterns discussed in the text.

in which $\mathbf{U}_{r2}$, commonly known as the Lagrangian-averaged residual flow (first-order approximation), should integrate to zero over a given cross section of the inlet based on conservation of mass. Although the Lagrangian residual is useful for examining fluid fluxes and transport, it is less relevant to near-bed sediment transport.

Simulations of spring-tide large-wave conditions were conducted with M2 tidal forcing (amplitude 0.78 m) and an offshore significant wave height of 3.1 m approaching the shore from the southeast (110° from the north). The modeled Eulerian residual flow velocity U_{r1} exceeds 0.5 m/s in the southwestern channel just offshore of the entrance to the ebb tidal delta (Figure 12a). The residual flow velocity over the ebb tidal delta is about 0.3 m/s. On the southwest side of the ebb tidal delta, a clockwise circulation pattern is predicted (see region III in Figure 12a), which feeds (or is adjacent to) a strong southwestward directed alongshore current driven by the oblique waves. Another clockwise circulation pattern appears off the northeastern shore (see region I in Figure 12a), which also is visible in the snapshots of maximum flood and ebb flows (Figures 3a and 3b). Over the center of the ebb tidal delta, the residual flow is landward-directed with a magnitude exceeding 0.25 m/s (region II in Figure 12a), although seaward-directed flow prevails in

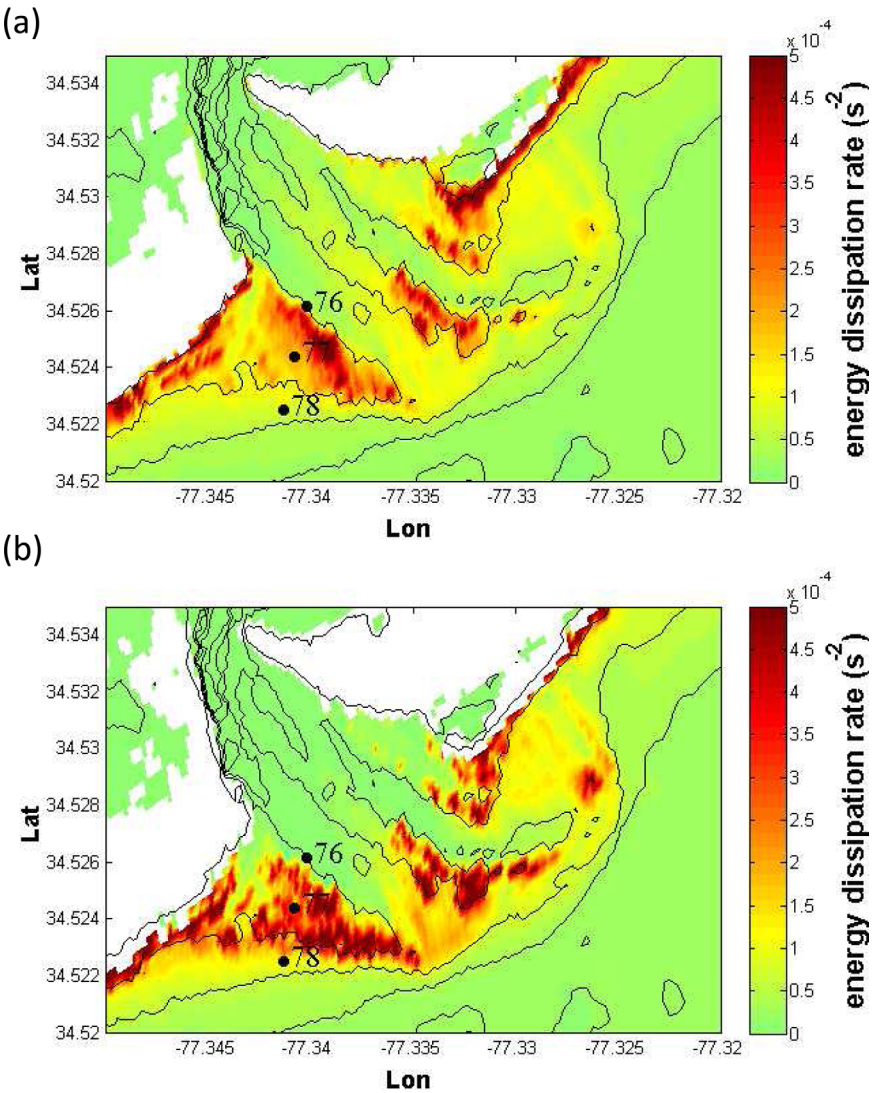

Figure 11. The rate of energy dissipation (color scale on the right) during (a) the maximum flood and (b) the maximum ebb for the spring tide-mild wave condition (Figure 8). The solid curves are bathymetric contours (0, 2, 4, 6, and 8 m depth relative to NAVD88).

the two channels. The calculated Lagrangian residual flow patterns ($\mathbf{U}_{r2}$, not shown) are qualitatively similar to those of the Eulerian residual flows ($\mathbf{U}_{r1}$). However, the Lagrangian magnitude is smaller than $\mathbf{U}_{r1}$ in the two inlet channels, and is much larger than $\mathbf{U}_{r1}$ on the shoals (owing to the weighting by water depth to conserve mass).

These complicated residual circulation patterns are caused by interactions between tidal currents, waves, and bathymetry. To isolate the effects of waves and tides, simulations were conducted with tidal forcing (M2 tidal amplitude 0.78 m), but without waves (Figure 12b) and with waves, but without tides (Figure 12c). The modeled residual flow near the entrances of the channels is weaker when wave effects are excluded (velocity magnitude reduces from about 0.5 m/s in Figure 12a to about 0.3 m/s in Figure 12b). Without waves, residual flows outside the channels are weak and the circulation patterns noted earlier are absent (compare Figure 12b with 12a in regions I and III). Furthermore, when the wave effects are excluded, the residual flow between the channels is seaward, rather than shoreward when waves are included (compare Figure 12b with 12a in region II).

When the model is forced solely by waves (without tidal flows), the simulated circulation patterns near the entrance and two sides of the inlet are similar, but more intense than those modeled with both tides and waves (compare Figure 12c with 12a). Thus, the model suggests that the clockwise circulation patterns on

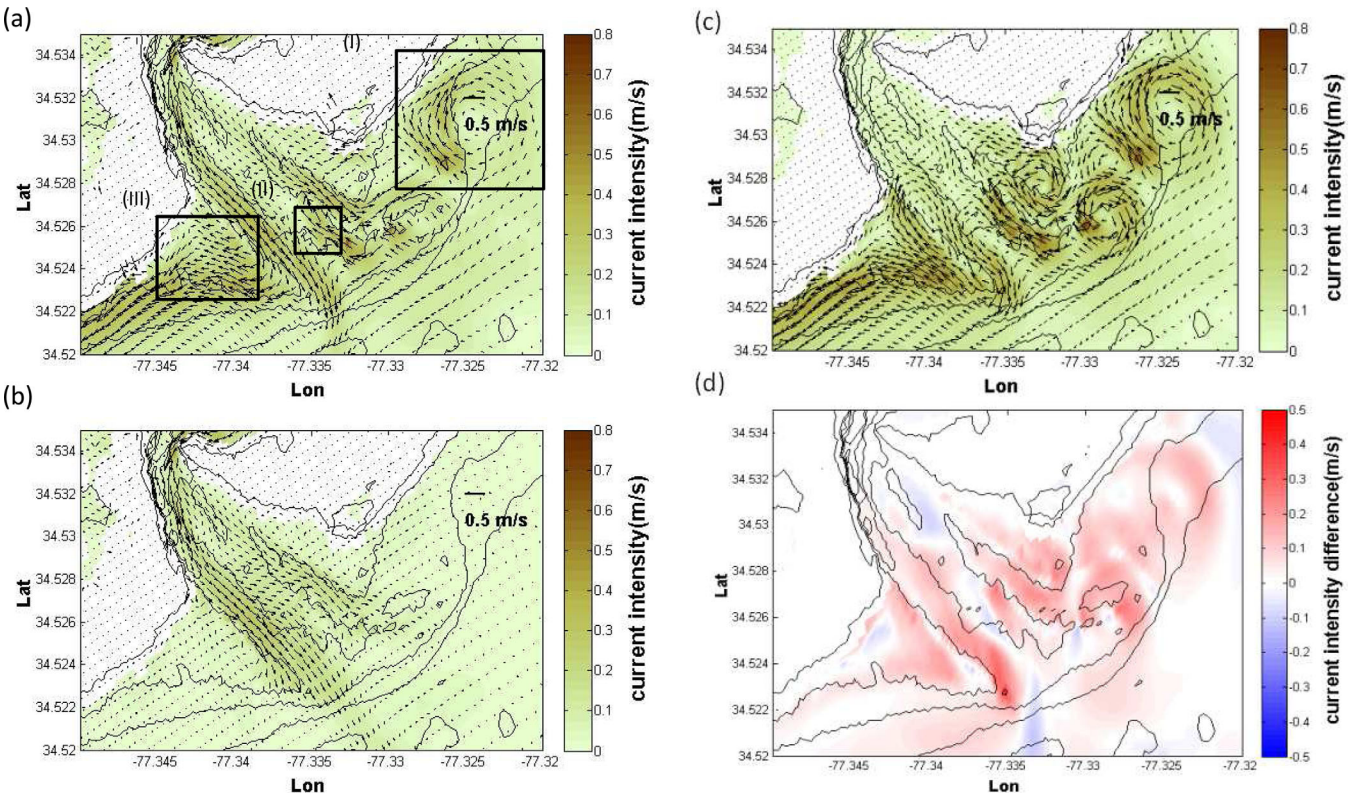

Figure 12. (a) Tidally averaged residual flow field of a spring tide-stormy wave condition (forced by a representative M2 tide). Box (I) indicates a clockwise circulation on the northeastern shore. Box (II) signifies an onshore residual flow near the center of ebb tidal delta. Box (III) shows a meandering residual flow pattern in the deeper channel and the south side of the ebb tidal delta. (b) The residual flow field driven only by tidal forcing (no waves). (c) Flow field driven by waves only (no tide). (d) The superposition of modeled velocities driven only by tides (b) and velocities driven only by waves (c) is subtracted from the modeled velocities driven by both tidal and wave forcing (a). Larger velocity differences (red contours) indicate greater importance of nonlinearity under wave-current interaction. The solid curves are bathymetric contours (0, 2, 4, 6, and 8 m depth relative to NAVD88).

both sides of the inlet and the landward-directed flow over the center of the ebb tidal delta are associated with interactions between the waves and bathymetry. These flow patterns are similar to the rip currents observed in many coastal systems, with offshore-directed flows in the deeper channels and landward-directed flows on the shallower shoals [see also *Olabarrieta et al*., 2014]. The simulated flow patterns are more complicated than those for the idealized system [*Olabarrieta et al*., 2014] owing to the complex channel-shoal and alongshore geometries at New River Inlet. Thus, in the simulation with both tidal and wave forcing (Figure 12a), the offshore-directed tidal residual velocities in the channels (Figure 12b) can be enhanced by rip currents (Figure 12c), while the wave forcing attenuates, or even reverses, the offshore flows near the center of the ebb tidal delta. Rip current circulation patterns depend on wave height, period, and direction, as well as bathymetry [*MacMahan et al*., 2006; *Dalrymple et al*., 2011]. Here, numerical experiments with nearly normally incident waves suggest that the wave-induced circulation patterns become insignificant (less than 0.1 m/s) when the offshore significant wave height is less than about 1 m. Similarly, rip current circulation patterns observed on an open coast beach in Monterey, CA were significant only when normally incident waves in 13 m depth were greater than 1 m [*MacMahan et al*., 2010]. The southeasterly waves also shift the direction of the modeled residual flow jet toward the west (compare the jet direction in Figure 12a with that in Figure 12b).

The model results suggest that waves play a vital role in generating the circulation patterns observed near the entrance of New River Inlet. To investigate the importance of nonlinear interactions between waves, currents, and bathymetry, the magnitudes of the vector sum of circulation velocities obtained from tide-only (Figure 12b) and wave-only (Figure 12c) forcing are subtracted from the magnitudes of the circulation velocity with combined tide and wave forcing (Figure 12a). The resulting velocity magnitude differences are spatially variable (Figure 12d). In the channels, nonlinear interactions reduce the magnitude of

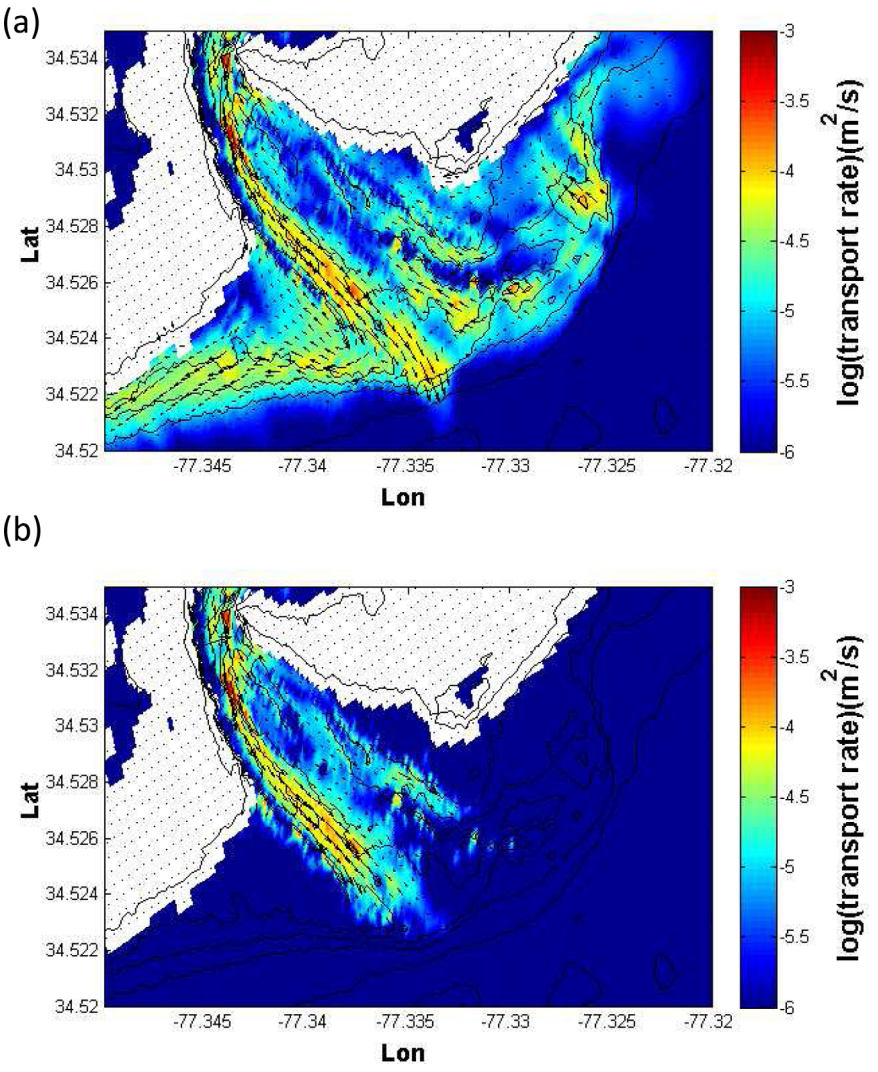

Figure 13. (a) Tidally averaged residual sediment fluxes for a spring tide-large wave condition with waves incident from the east-southeast. Vectors indicate direction and color contours (scale on the right) indicate the magnitude of sediment fluxes. (b) Tidally averaged residual sediment fluxes for a spring tide condition without waves. The solid curves are bathymetric contours (0, 2, 4, 6, and 8 m depth relative to NAVD88).

seaward-directed residual flows, which can be overestimated by about 50% (~0.2 m/s) if nonlinear effects are neglected (Figure 12d). Near the center and around the two edges of the ebb tidal delta, neglecting nonlinear effects leads to errors in current magnitudes of up to 0.2 m/s (i.e., onshore flows are overestimated if nonlinear effects are neglected) (Figure 12d). The largest errors associated with neglecting nonlinearities occur where rip structures are simulated owing to wave-bathymetry-current interactions that tend to attenuate the flow intensity and shift the direction of the flow jet.

5.3. Sediment Transport

The importance of wave-current interactions to sediment transport and morphological change is investigated by simulating the tidally averaged residual sediment fluxes for the spring tide-large wave condition using a total load sediment transport formula (equation (12)) [*Soulsby*, 1997]. For simplicity, the tidal forcing is approximated using only the M2 constituent and the sediment grain size is approximated as d_{50}=0.2 mm over the entire domain.

The modeled residual sediment fluxes are offshore directed in the channels, with significant transport extending offshore of the 6 m bathymetric contour (Figure 13a). On the ebb tidal delta, sediment flux patterns are more complicated. The residual circulation pattern on the northeastern side of the inlet (region I

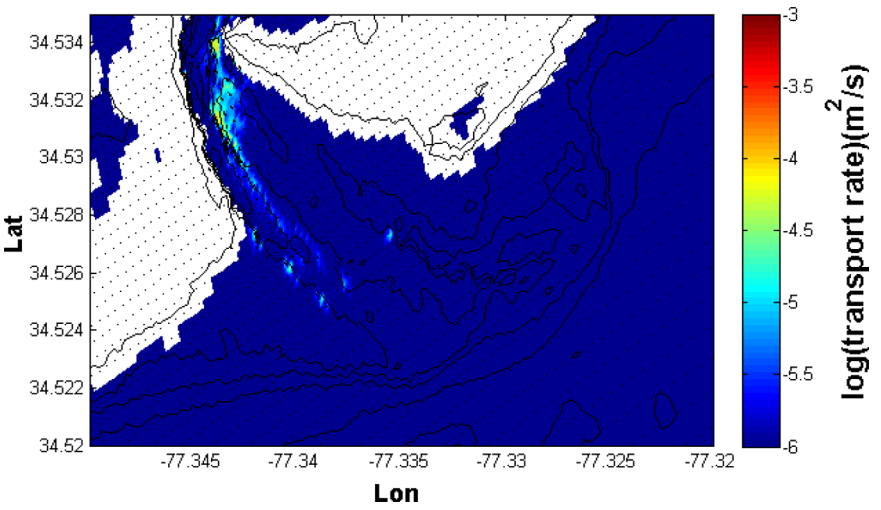

Figure 14. Tidally averaged residual sediment fluxes for a neap tide condition without waves. Vectors indicate direction and color contours (scale on the right) indicate the magnitude of sediment fluxes. The solid curves are bathymetric contours (0, 2, 4, 6, and 8 m depth relative to NAVD88).

in Figure 12a) affects the sediment fluxes. However, the patterns of the residual flow and sediment transport differ because the threshold velocity owing to combined waves and currents (needed to initiate sediment movement) is not always exceeded for the grain size used here. Near the center of the ebb tidal delta, sediment fluxes are landward directed, consistent with the residual flow (region II in Figure 12a). On the southwest edge of the ebb tidal delta, sediment transport roughly follows the 2 m depth contour, and becomes approximately parallel to the beach at the southwest edge of the domain (Figure 13a). Immediately southwest of the southwestern (deeper) channel, however, sediment flux on the ebb tidal delta is landward-directed.

When waves are neglected in the simulations, the modeled residual sediment fluxes during a spring tide condition are ebb (seaward) dominant in the channels and are negligible on the south side and center of the ebb tidal delta, and along the southwestern and northeastern shore (Figure 13b). For a tidal amplitude half that of the spring tide condition (amplitude 0.39 m represents a neap tide condition), residual sediment fluxes in the channel are lower than 10^{-5} m^2/s (Figure 14), which is at least one-order magnitude smaller than those during a spring tide condition (Figure 13b). Thus, the simulations suggest that the ebb-dominant tidal jet results in offshore transport in the channel, whereas the circulation patterns resulting from waves and wave-current-bathymetry interactions (section 5.2) may carry sediment landward or alongshore on the ebb tidal delta.

In the combined wave-and-tide case, the simulated offshore transport extends farther offshore (owing to wave stirring), and the sediment fluxes near the entrance of the channels are an order of magnitude larger than those when wave effects are not included (compare Figure 13a with 13b). On the southwest edge of the ebb tidal delta near the 2 m depth contour, sediment fluxes in the east-west direction are as high as 10^{-4} m^2/s, which is one-order magnitude larger than those in the north-south direction, and are consistent with the southeasterly wave direction and the resulting southwesterly wave-driven alongshore currents. Including wave forcing may result in increased seabed changes near the center and along the offshore edge on the southwestern side of the ebb shoal. These results in New River Inlet are similar to those in Teign Inlet, UK, where the sediment transport in the channels is dependent on tides (spring tide), but the transport on the ebb tidal delta primarily is owing to waves [*Siegle et al.*, 2004].

Energetic waves at New River Inlet can be incident from the southwest, as well as from the southeast, and simulations suggest sediment fluxes are dependent on the wave direction (Figure 15, tidal amplitude and significant wave heights are identical to those in Figure 13a, but with a south-southwest incident wave direction). When waves are incident from the southwest, there is no southwestward directed alongshore transport on the southwest edge of the ebb tidal delta (Figure 15). In addition, waves from the southwest result in onshore transport, which may cause seabed accretion on the southwestern side of the ebb delta (depths < 2 m). The

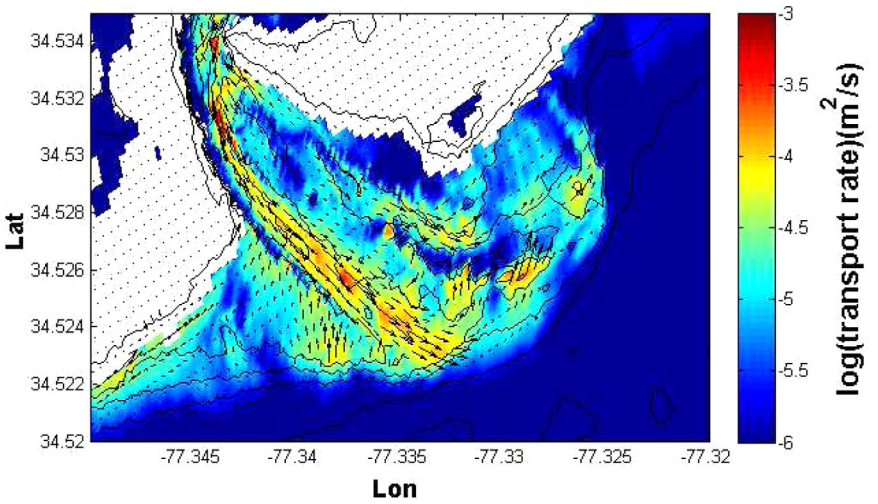

Figure 15. Tidally averaged residual sediment fluxes for a spring tide-large wave condition with waves incident from the south-southwest. Vectors indicate direction and color contours (scale on the right) indicate the magnitude of sediment fluxes. The solid curves are bathymetric contours (0, 2, 4, 6, and 8 m depth relative to NAVD88).

northerly transport across the ebb delta may result in erosion near the center of the ebb delta and along the southern edge of the shallow channel. Sediment transport at the offshore end of the deeper channel is easterly (rather than southerly as it is for southeast waves), with the resulting accretion primarily onshore of the 4 m contour and on the northern edge of the channel. The transport and accretion patterns at the offshore end of the channel could be owing to wave-driven shifting of the flow direction in the ebb jet.

6. Conclusions

Hydrodynamics and sediment transport in New River Inlet, NC were investigated using NearCoM-TVD [*Shi et al.*, 2003; *Chen et al.*, 2014], which consists of a new version of the quasi-3-D nearshore circulation model SHORECIRC coupled with the spectral wave model SWAN. The numerical model was validated with observations from 30 colocated wave and current sensors during a 1 month long field experiment that included spring and neap tides and a range of wave conditions (offshore significant wave heights between 0.5 and 3.1 m). The numerical model reproduces the waves and circulation observed throughout the nearshore and the inlet, including in two channels and on the ebb tidal delta. Both the observations and simulations show a narrow (few hundred meters) transition between the current-dominated and wave-dominated processes over the ebb tidal delta. The simulations suggest this transition region occurs over the narrow breaker zone, which is modulated by tidal water depth fluctuations.

The validated model is used to examine the complex hydrodynamic patterns of the inlet-bay-beach system. The circulation patterns observed at New River Inlet may differ from prior model simulations of Ria de Ribadeo, Spain [*Piedracoba et al.*, 1999] and Willapa Bay Inlet, WA [*Olabarrieta et al.*, 2011] owing to differences in the inlet and bay geometries and the complex channel-shoal bathymetries [*Wargula et al.*, 2014]. Comparing simulation results with tidal-flow-forcing only with results for wave-forcing only suggests that waves play an important role in the generation of tidally averaged (residual) circulation patterns near the inlet entrance, enhancing offshore-directed flow in the channels and driving landward-directed currents over the ebb tidal delta. The interactions between waves and bathymetry that cause these residual flow patterns are similar to those in rip-current systems with alongshore "feeder" currents close to shore, onshore flows over the shoals, and offshore flows in the channels [see also *Olabarrieta et al.*, 2014]. Moreover, magnitudes of the residual currents resulting from combined wave-forcing and tide-forcing typically are smaller than those calculated from a linear superposition of flows driven by tide-only and wave-only forcing, suggesting that nonlinear wave-current-bathymetry interactions are important.

Tidally averaged residual sediment fluxes are estimated by coupling NearCoM-TVD with a total load sediment transport formula [*Soulsby*, 1997]. Model sediment fluxes and patterns of accretion and erosion when

waves are included differ from those when waves are neglected. During a spring-tide large-wave condition with waves incident from the southeast, sediment flux in the southwestern (deeper) channel is enhanced seaward of the ebb shoal (extending beyond the 6 m bathymetric contour), relative to the flux simulated without waves. Waves also induce significant sediment fluxes and seabed change on the ebb tidal delta and adjacent shore. However, when waves are incident from the southwest, the enhanced transport in the adjacent ebb tidal delta is less significant. Thus, the simulations suggest tidal amplitude, wave intensity, and wave direction all influence the morphodynamics of New River Inlet.

Acknowledgments

The field observations and numerical results presented in this manuscript are available upon request from Jia-Lin Chen (jialin@udel.edu), Tian-Jian Hsu (thus@udel.edu), Fengyan Shi (fyshi@udel.edu), Britt Raubenheimer (braubenheimer2@whoi.edu), and Steve Elgar (elgar@whoi.edu). Funding was provided by the Office of Naval Research (N00014-13-1–0120 and N00014-14-1-0586) and the Office of the Assistant Secretary of Defense for Research and Engineering. We thank Jesse McNinch for New River Inlet bathymetry, Ad Reiners, and Jamie MacMahan for backbay bathymetry, Jim Thomson for wind measurements, and the PVLAB field crew and staff of the USACE Field Research Facility for deploying, maintaining, and recovering the field instrumentation.

References

Bertin, X., A. B. Fortunato, and A. Oliveira, A., (2009), A modelling-based analysis of processes driving wave-dominated inlets, *Cont. Shelf Res.*, *29*, 819–834.

Booij, N., R. C. Ris, and L. H. Holthuijsen (1999), A third-generation wave model for coastal regions, *J. Geophys. Res.*, *104*, 7649–7666.

Chen, J.-L., F. Shi, T.-J. Hsu, and J. T. Kirby (2014), NEARCOM-TVD: A quasi-3D nearshore circulation and sediment transport model, *Coastal Eng.*, *91*, 200–212.

Chen, J.-L., T.-J. Hsu, F. Shi, B. Raubenheimer, and S. Elgar (2014), Hydrodynamic Modeling of New River Inlet, North Carolina Using Near-com-TVD, *Coastal Engineering Proceedings*, *1*(34), currents. 41, doi:10.9753/icce.v34.currents.41.

Dalrymple, R. A., J. H. MacMahan, A. J. H. M. Reniers, and V. Nelko (2011), Rip currents, *Annu. Rev. Fluid Mech.*, *43*, 551–581.

de Swart H. E., and J. T. F. Zimmerman (2009), Morphodynamics of tidal inlet systems, *Annu. Rev. Fluid Mech.*, *41*, 203–229.

Dodet, G., X. Bertin, N. Bruneau, A. Fortunato, A. Nahon, and A. Roland (2013), Wave- current interactions in a wave-dominated tidal inlet, *J. Geophys. Res. Oceans*, *118*, 1587–1605, doi:10.1002/jgrc.20146.

Elias, E. P. L., J. Cleveringa, M. C. Buijsman, J. A. Roelvink, and M. J. F. Stive (2006), Field and model data analysis of sand transport patterns in Texel tidal inlet, *Coastal Eng.*, *53*, 505–529.

Grant, W. D., and O. S. Madsen (1979), Combined wave and current interaction with a rough bottom, *J. Geophys. Res.*, *89*, 1797–1808.

Haas, K. A., and J. C. Warner (2009), Comparing a quasi-3D to a full 3D nearshore circulation model: SHORECIRC and ROMS, *Ocean Modell.*, *26*(1–2), 91–103.

Hench, J. L., and R. A. Luettich Jr. (2003), Transient tidal circulation and momentum balances at a shallow inlet, *J. Phys. Oceanogr.*, *33*, 913–932.

Inman, D. L., and B. M. Brush (1973), Coastal challenge, *Science*, *181*, 20–32.

Keshtpoor, M., J. Puleo, F. Shi, and N. DiCosmo (2014), Numerical simulation of nearshore hydrodynamics and sediment transport down-drift of a tidal inlet, *J. Waterw. Port Coastal Ocean Eng.*, *141*(2), 04014035.

Keulegan, G. H. (1967), Tidal flow in entrances: Water level fluctuations of basins in communication with the seas, in *Committee on Tidal Hydraulics*, *Tech. Bull. 14*, U.S. Army Eng. Waterways Exp. Stn., Vicksburg, Miss.

Kumar, N., G. Voulgaris, and J. C. Warner (2011), Implementation and modification of a three-dimensional radiation stress formulation for surf zone and rip-current applications, *Coastal Eng.*, *58*, 1097–1117.

Longuet-Higgins, (1969), On the transport of mass by time-varying ocean currents, *Deep Sea Res. Oceanogr. Abstr.*, *16*, 437–447.

Longuet-Higgins, M. S., and R. W. Stewart (1962), Radiation stress and mass transport in gravity waves, with application to 'surf beats', *J. Fluid Mech. 13*(4), 481–504.

Longuet-Higgins, M. S., and R. W. Stewart (1964), Radiation stresses in water waves; A physical discussion, with applications, *Deep Sea Res. Oceanogr. Abstr.*, 529–562.

Luettich, R. A. and J. J. Westerink (1991), A solution for the vertical variation of stress, rather than velocity, in a three-dimensional circulation model, *Int. J. Numer. Methods Fluids*, *12*, 911–928.

MacMahan, J., E. B. Thornton, and A. J. H. M. Reniers (2006), Rip current review, *Coastal Eng.*, *53*, 191–208.

MacMahan, J., et al. (2010), Mean Lagrangian flow behavior on an open coast rip channeled beach: A new perspective, *Mar. Geol.*, *268*, 1–15.

MacMahan, J., J. van de Kreeke, A. Reniers, S. Elgar, B. Raubenheimer, E. Thornton, M. Weltmer, P. Rynne, and J. Brown (2014), Fortnightly tides and subtidal motions in a choked inlet, *Estuarine Coastal Shelf Sci.*, vol. 150, Part B, 5 October, pp. 5–331.

Malhadas, M. S., P. C. Leitao, A. Silva, and R. Neves (2009), Effect of coastal waves on sea level in Óbidos Lagoon, Portugal, *Cont. Shelf Res.*, *19*(9), 1240–1250.

Mellor, G., (2005), Some consequences of the three-dimensional current and surface wave equations, *J. Phys. Oceanogr.*, *35*, 2291–2298.

Newberger, P. A., and J. S. Allen (2007), Forcing a three dimensional, hydrostatic primitive- equation model for application in the surf zone: 1. Formulation, *J.Geophys. Res.*, *112*, C08018, doi:10.1029/2006JC003472.

Nidzieko, N. J., and D. K. Ralston (2011), Tidal asymmetry and velocity skew over tidal flats and shallow channels within a macrotidal river delta, *J. Geophys. Res.*, *117*, C03001, doi:10.1029/2011JC007384.

Olabarrieta, M., J. C. Warner, and N. Kumar (2011), Wave-current interaction in Willapa Bay, *J. Geophys. Res.*, *116*, C12014, doi:10.1029/2011JC007387.

Olabarrieta, M., W. R. Geyer, and N. Kumar (2014), The role of morphology and wave-current interaction at tidal inlets: An idealized modeling analysis, *J. Geophys. Res. Oceans*, *119*, 8818–8837, doi:10.1002/2014JC010191.

Orescanin, M., B. Raubenheimer, and S. Elgar (2014), Observations of wave effects on inlet circulation, *Cont. Shelf Res.*, *82*, 37–42.

Piedracoba, S., C. Souto, M. Gilcoto, P. C. Pardo, (2005), Hydrography and dynamics of the Ría de Ribadeo (NW Spain), a wave driven estuary, Estuarine, *Coastal and Shelf Science*, *65*, pp. 726–738, doi:10.1016/j.ecss.2005.07.013.

Pilkey, O. H., W. J. Neal, S. R. Riggs, and C. A. Webb (1998), *The North Carolina and Its Barrier Islands: Restless Ribbons of Sand*, pp. 61–86, Duke Univ. Press Books, Durham, N. C.

Putrevu, U., and I. A. Svendsen (1999), Three-dimensional dispersion of momentum in wave induced nearshore currents, *Eur. J. Mech. B/Fluids*, *18*, 409–427.

Rogowski, P., E. Terrill, and J. Chen (2014), Observations of the frontal region of a buoyant river plume using an autonomous underwater vehicle, *J. Geophys. Res. Oceans*, *119*, 7549–7567, doi:10.1002/2014JC010392.

Shepard, F. P., K. O. Emery, and E. C. La Fond (1941), Rip currents: A process of geological importance, *J. Geol.*, *49*, 337–369.

Shi, F., I. A. Svendsen, J. T. Kirby, and J. M. Smith (2003), A curvilinear version of a Quasi-3D nearshore circulation model, *Coastal Eng.*, *49*(1–2), 99–124.

Shi, F., D. M. Hanes, J. T. Kirby, L. Erikson, P. Barnard, and J. Eshleman (2011), Pressure gradient driven nearshore circulation on a beach influenced by a large inlet-tidal shoal system, *J. Geophys. Res.*, *116*, C04020, doi:10.1029/2010JC006788.
Shi, F., G. Vittori, and J. T. Kirby (2015), Concurrent correction method for modeling morphological response to dredging an offshore sand-pit, *Coastal Eng.*, *97*, 1–10.
Siegle, E., D. A. Huntley, and M. A. Davidson (2004), Physical controls on the dynamics of inlet sandbar systems, *Ocean Dyn.*, *54*(3–4), 360–373.
Smith, J., H. Bermudez, and B. Ebersole. (2001), Modeling Waves at Willapa Bay, Washington. Coastal Engineering 2000, pp. 826–839, doi: 10.1061/40549(276)64.
Smith, J. M., H. E. Bermudez, and B. A. Ebersole (2000), Modeling waves at Willapa Bay, Washington, in *Proceedings of the 27th International Conference on Coastal Engineering*, pp. 826–839, Am. Soc. of Civ. Eng.
Soulsby, R. L. (1997), *Dynamics of Marine Sands*, pp. 182–185, Thomas Telford, London, U. K.
Svendsen, I. A., and U. Putrevu (1990), Nearshore circulation with 3-D profiles, in *Proceedings of the 22th International Conference on Coastal Engineering*, pp. 241–254, Am. Soc. of Civ. Eng.
Soulsby, R. L., L. Hamm, G. Klopman, D. Myrhaug, R. R. Simons, and G. P. Thomas (1993), Wave-Current Interaction within and outside the bottom boundary layer, *Coastal Eng.*, *21*, 41–69.
Svendsen, I. A., K. Haas, and Q. Zhao (2002), Quasi-3D nearshore circulation model SHORECIRC: Version 2.0, CACR-02-01 research report, Cent. for Appl. Coastal Res., Univ. of Delaware.
Svendsen, I., and U. Putrevu (2011), NEARSHORE CIRCULATION WITH 3-D PROFILES. *Coastal Engineering Proceedings*, *1*(22).
Swart, D. H. (1974), *Offshore sediment transport and equilibrium beach profiles, Rep. 131*, 217 pp., Delft Hydraulic Lab., Delft, Netherlands.
Toro, E. F. (2009), *Riemann Solvers and Numerical Methods for Fluid Dynamics: A Practical Introduction*, 3rd ed., Springer, N. Y.
Uncles R. J., and M. B. Jordan (1980), A one-dimensional representation of residual currents in the Severn estuary and associated observations, *Estuarine Coast Mar. Sci.*, *10*, 39–60.
Van Dorn, W. C. (1953), Wind stress on an artificial pond, pp. 249–276, *J. Mar. Res.*, *12*.
van Rijn, L. C. (1984), Sediment transport, part III: Bed forms and alluvial roughness, *J. Hydrual. Eng, ASCE*, *110*(12), 1733–1754.
Warner, J. C., C. R. Sherwood, R. P. Signell, C. K. Harris, and H. G. Arango (2008), Development of a three-dimensional, regional, coupled wave, current, and sediment-transport model, *Comput. Geosci.*, *34*(10), 1284–1306.
Wargula, A., B. Raubenheimer, and S. Elgar (2014), Wave-driven along-channel subtidal flows in a well-mixed ocean inlet, *J. Geophys. Res. Oceans*, *119*, 2987–3001, doi:10.1002/2014JC009839.
Wolf, J., and D. Prandle (1999), Some observations of wave–current interaction, *Coastal Eng.*, *371*, 471–485.